# Terahertz imaging of metastatic lymph nodes using spectroscopic integration technique

**JAE YEON PARK,[1] HYUCK JAE CHOI,[2] HWAYEONG CHEON,[1] SEONG WHI CHO,[2] SEUNGKOO LEE,[3] AND JOO-HIUK SON[1,*]**

[1]*Department of Physics, University of Seoul, Seoul 130- 743, South Korea*
[2]*Department of Radiology, Kangwon National University Hospital, Chuncheon, South Korea*
[3]*Department of Anatomic Pathology, Kangwon National University Hospital, Chuncheon, South Korea*
*[*]joohiuk@uos.ac.kr*

**Abstract:** Terahertz (THz) imaging was used to differentiate the metastatic states of frozen lymph nodes (LNs) by using spectroscopic integration technique (SIT). The metastatic states were classified into three groups: healthy LNs, completely metastatic LNs, and partially metastatic LNs, which were obtained from three mice without infection and six mice infected with murine melanoma cells for 30 days and 15 days, respectively. Under histological examination, the healthy LNs and completely metastatic LNs were found to have a homogeneous cellular structure but the partially metastatic LNs had interfaces of the melanoma and healthy tissue. THz signals between the experimental groups were not distinguished at room temperature due to high attenuation by water in the tissues. However, a signal gap between the healthy and completely metastatic LNs was detected at freezing temperature. The signal gap could be enhanced by using SIT that is a signal processing method dichotomizing the signal difference between the healthy cells and melanoma cells with their normalized spectral integration. This technique clearly imaged the interfaces in the partially metastatic LNs, which could not be achieved by existing methods using a peak point or spectral value. The image resolution was high enough to recognize a metastatic area of about 0.7 mm size in the partially metastatic LNs. Therefore, this pilot study demonstrated that THz imaging of the frozen specimen using SIT can be used to diagnose the metastatic state of LNs for clinical application.

## References and links

1. D. N. Krag, S. J. Anderson, T. B. Julian, A. M. Brown, S. P. Harlow, J. P. Costantino, T. Ashikaga, D. L. Weaver, E. P. Mamounas, L. M. Jalovec, T. G. Frazier, R. D. Noyes, A. Robidoux, H. M. Scarth, and N. Wolmark, "Sentinel-lymph-node resection compared with conventional axillary-lymph-node dissection in clinically node-negative patients with breast cancer: overall survival findings from the NSABP B-32 randomised phase 3 trial," Lancet Oncol. **11**(10), 927–933 (2010).
2. J. E. Gershenwald and M. I. Ross, "Sentinel-lymph-node biopsy for cutaneous melanoma," N. Engl. J. Med. **364**(18), 1738–1745 (2011).
3. M. Salhab, N. Patani, and K. Mokbel, "Sentinel lymph node micrometastasis in human breast cancer: an update," Surg. Oncol. **20**(4), e195–e206 (2011).
4. T. H. Cheung, W. K. Lo, M. Y. Yu, W. T. Yang, and S. Ho, "Extended experience in the use of laparoscopic ultrasound to detect pelvic nodal metastasis in patients with cervical carcinoma," Gynecol. Oncol. **92**(3), 784–788 (2004).
5. A. D. Williams, C. Cousins, W. P. Soutter, M. Mubashar, A. M. Peters, R. Dina, F. Fuchsel, G. A. McIndoe, and N. M. deSouza, "Detection of pelvic lymph node metastases in gynecologic malignancy: a comparison of CT, MR imaging, and positron emission tomography," AJR Am. J. Roentgenol. **177**(2), 343–348 (2001).
6. M. Bellomi, G. Bonomo, F. Landoni, G. Villa, M. E. Leon, L. Bocciolone, A. Maggioni, and G. Viale, "Accuracy of computed tomography and magnetic resonance imaging in the detection of lymph node involvement in cervix carcinoma," Eur. Radiol. **15**(12), 2469–2474 (2005).
7. H. J. Choi, J. W. Roh, S.-S. Seo, S. Lee, J.-Y. Kim, S.-K. Kim, K. W. Kang, J. S. Lee, J. Y. Jeong, and S.-Y. Park, "Comparison of the accuracy of magnetic resonance imaging and positron emission tomography/computed tomography in the presurgical detection of lymph node metastases in patients with uterine cervical carcinoma: a prospective study," Cancer **106**(4), 914–922 (2006).

8.  W. T. Yang, W. W. M. Lam, M. Y. Yu, T. H. Cheung, and C. Metreweli, "Comparison of dynamic helical CT and dynamic MR imaging in the evaluation of pelvic lymph nodes in cervical carcinoma," AJR Am. J. Roentgenol. **175**(3), 759–766 (2000).
9.  H.-H. Chou, T.-C. Chang, T.-C. Yen, K.-K. Ng, S. Hsueh, S.-Y. Ma, C.-J. Chang, H. J. Huang, A. Chao, T.-I. Wu, S.-M. Jung, Y.-C. Wu, C.-T. Lin, K.-G. Huang, and C.-H. Lai, "Low value of [18F]-fluoro-2-deoxy-D-glucose positron emission tomography in primary staging of early-stage cervical cancer before radical hysterectomy," J. Clin. Oncol. **24**(1), 123–128 (2006).
10. E.-A. Jung, M.-H. Lim, K.-W. Moon, Y.-W. Do, S.-S. Lee, H.-W. Han, H.-J. Choi, K.-S. Cho, and K.-R. Kim, "Terahertz pulse imaging of micro-metastatic lymph nodes in early-stage cervical cancer patients," J. Opt. Soc. Korea **15**(2), 155–160 (2011).
11. Y. C. Sim, J. Y. Park, K.-M. Ahn, C. Park, and J.-H. Son, "Terahertz imaging of excised oral cancer at frozen temperature," Biomed. Opt. Express **4**(8), 1413–1421 (2013).
12. Y. C. Sim, K.-M. Ahn, J. Y. Park, C.-S. Park, and J.-H. Son, "Temperature-dependent terahertz imaging of excised oral malignant melanoma," IEEE J. Biomed. Health Inform. **17**(4), 779–784 (2013).
13. R. M. Woodward, B. E. Cole, V. P. Wallace, R. J. Pye, D. D. Arnone, E. H. Linfield, and M. Pepper, "Terahertz pulse imaging in reflection geometry of human skin cancer and skin tissue," Phys. Med. Biol. **47**(21), 3853–3863 (2002).
14. A. J. Fitzgerald, V. P. Wallace, M. Jimenez-Linan, L. Bobrow, R. J. Pye, A. D. Purushotham, and D. D. Arnone, "Terahertz pulsed imaging of human breast tumors," Radiology **239**(2), 533–540 (2006).
15. J.-H. Son, "Terahertz electromagnetic interactions with biological matter and their applications," J. Appl. Phys. **105**(10), 102033 (2009).
16. S. J. Oh, J. Kang, I. Maeng, J.-S. Suh, Y.-M. Huh, S. Haam, and J.-H. Son, "Nanoparticle-enabled terahertz imaging for cancer diagnosis," Opt. Express **17**(5), 3469–3475 (2009).
17. J.-H. Son, "Principle and applications of terahertz molecular imaging," Nanotechnology **24**(21), 214001 (2013).
18. Y. B. Ji, C. H. Park, H. Kim, S.-H. Kim, G. M. Lee, S. K. Noh, T.-I. Jeon, J.-H. Son, Y.-M. Huh, S. Haam, S. J. Oh, S. K. Lee, and J.-S. Suh, "Feasibility of terahertz reflectometry for discrimination of human early gastric cancers," Biomed. Opt. Express **6**(4), 1398–1406 (2015).
19. C. Ronne, R.-O. Astrand, A. Wallqvist, K. V. Mikkelsen, and S. R. Keiding, "Investigation of the temperature dependence of dielectric relaxation in liquid water by THz reflection spectroscopy and molecular dynamics simulation," J. Chem. Phys. **107**(14), 5319–5331 (1997).
20. S. J. Oh, S.-H. Kim, K. Jeong, Y. Park, Y.-M. Huh, J.-H. Son, and J.-S. Suh, "Measurement depth enhancement in terahertz imaging of biological tissues," Opt. Express **21**(18), 21299–21305 (2013).
21. Y. Miura, A. Kamataki, M. Uzuki, T. Sasaki, J. Nishizawa, and T. Sawai, "Terahertz-wave spectroscopy for precise histopathological imaging of tumor and non-tumor lesions in paraffin sections," Tohoku J. Exp. Med. **223**(4), 291–296 (2011).
22. J. Y. Park, H. J. Choi, K.-S. Cho, K.-R. Kim, and J.-H. Son, "Terahertz spectroscopic imaging of a rabbit VX2 hepatoma model," J. Appl. Phys. **109**(6), 064704 (2011).
23. S. J. Oh, S.-H. Kim, Y. B. Ji, K. Jeong, Y. Park, J. Yang, D. W. Park, S. K. Noh, S.-G. Kang, Y.-M. Huh, J.-H. Son, and J.-S. Suh, "Study of freshly excised brain tissues using terahertz imaging," Biomed. Opt. Express **5**(8), 2837–2842 (2014).
24. P. C. Ashworth, E. Pickwell-MacPherson, E. Provenzano, S. E. Pinder, A. D. Purushotham, M. Pepper, and V. P. Wallace, "Terahertz pulsed spectroscopy of freshly excised human breast cancer," Opt. Express **17**(15), 12444–12454 (2009).
25. R. M. Woodward, V. P. Wallace, R. J. Pye, B. E. Cole, D. D. Arnone, E. H. Linfield, and M. Pepper, "Terahertz pulse imaging of ex vivo basal cell carcinoma," J. Invest. Dermatol. **120**(1), 72–78 (2003).
26. S. Fan, E. P. J. Parrott, B. S. Y. Ung, and E. Pickwell-MacPherson, "Calibration method to improve the accuracy of THz imaging and spectroscopy in reflection geometry," Photon. Res. **4**(3), A29–A35 (2016).
27. A. J. Fitzgerald, S. Pinder, A. D. Purushotham, P. O'Kelly, P. C. Ashworth, and V. P. Wallace, "Classification of terahertz-pulsed imaging data from excised breast tissue," J. Biomed. Opt. **17**(1), 016005 (2012).
28. Y. He, B. S.-Y. Ung, E. P. J. Parrott, A. T. Ahuja, and E. Pickwell-MacPherson, "Freeze-thaw hysteresis effects in terahertz imaging of biomedical tissues," Biomed. Opt. Express **7**(11), 4711–4717 (2016).
29. R. M. Woodward, B. E. Cole, V. P. Wallace, R. J. Pye, D. D. Arnone, E. H. Linfield, and M. Pepper, "Terahertz pulse imaging in reflection geometry of human skin cancer and skin tissue," Phys. Med. Biol. **47**(21), 3853–3863 (2002).
30. T. Löffler, K. Siebert, S. Czasch, T. Bauer, and H. G. Roskos, "Visualization and classification in biomedical terahertz pulsed imaging," Phys. Med. Biol. **47**(21), 3847–3852 (2002).
31. C. B. Reid, A. Fitzgerald, G. Reese, R. Goldin, P. Tekkis, P. S. O'Kelly, E. Pickwell-MacPherson, A. P. Gibson, and V. P. Wallace, "Terahertz pulsed imaging of freshly excised human colonic tissues," Phys. Med. Biol. **56**(14), 4333–4353 (2011).
32. K. W. Kim, K.-S. Kim, H. Kim, S. H. Lee, J.-H. Park, J.-H. Han, S.-H. Seok, J. Park, Y. Choi, Y. I. Kim, J. K. Han, and J.-H. Son, "Terahertz dynamic imaging of skin drug absorption," Opt. Express **20**(9), 9476–9484 (2012).
33. K. W. Kim, H. Kim, J. Park, J. K. Han, and J.-H. Son, "Terahertz tomographic imaging of transdermal drug delivery," IEEE Trans. Terahertz Sci. Technol. **2**(1), 99–106 (2012).

## 1. Introduction

Regional lymph node (LN) metastasis is an important cancer model, capturing the prognostic factors of malignant tumors for many malignancies [1–3]. For early detection of metastatic LNs, radiological imaging techniques such as X-ray computerized tomography (CT), positron emission tomography (PET), PET-CT, and magnetic resonance imaging (MRI) have been used [4–8]. Metastasis detection is crucial for correct surgery decisions. However, the detection rate using PET has been reported to be 10% [9], and MRI cannot be used for detecting metastatic LNs. The unsatisfactory performance of current imaging techniques follows because metastatic LNs have very small metastatic foci and yield low-discriminability signals. Conventional terahertz (THz) imaging is promising for achieving good imaging quality, as shown using paraffin-embedded LN models [10]. In addition, frozen THz imaging has been shown to successfully detect small signal differences between normal and cancerous oral tissues [11, 12]. These earlier studies suggest that THz imaging is promising for the diagnostics of metastatic LN cancer.

Several studies have suggested using THz imaging for cancer diagnostics [13–18]. Significant absorption of THz by tissue water was found to be key for discriminating between cancerous and intact cells, but precluded the analysis of the tissue bulk [19, 20]. To alleviate the absorption of THz by water molecules, the tissue is usually dehydrated and covered with paraffin. This model indicates that tissue properties affect the response to THz radiation, and these conclusions have been validated in image analysis studies [21–23]. This approach yields clear images of cancerous regions, but is time-consuming. In addition, tissue cells may interact with other embedded materials. Another approach has been to freeze the tissue, because water exhibits much weaker THz absorption at the freezing temperature while the tissue molecular structure is not affected by freezing [11, 12]. THz imaging using these methods enables mapping the peak values of THz time-domain waveforms or single THz spectral peaks corresponding to the refractive index and/or absorption [13, 24, 25]. Using suitable parameters and signal analysis methods, the accuracy of cancer demarcation has been improved [26, 27].

In the present work, we investigated the discriminability of metastatic excised LNs at room temperature and at the freezing temperature of water, using a novel signal processing technique that maximizes the difference between signals corresponding to intact and cancerous regions.

## 2. Experiments

All animal experiments were performed under sterile conditions, following the approval of our Institutional Animal Care and Use Committee (IACUC). Murine melanoma cells (B16F10) were grown on glass coverslips in McCoy's 5A medium supplemented with 10% (v/v) fetal bovine serum (FBS), 100 units/mL penicillin, and 100 µL/mL streptomycin, in an atmosphere that consisted of humidified air (95%) and $CO_2$ (5%) at 37 °C, until the exponential phase was attained. The melanoma cells were injected into six female BALB/c nude mice, aged 6–8 weeks, selected from the group of nine mice. The group of nine mice was divided into three groups, with three animals in each group. The control group animals had no melanoma cells, whereas the animals in the experimental groups were let to live with the injected melanoma cells for 15 days and 30 days. For analysis purposes, the LNs of the nine animals were excised and quickly frozen because the snap-freezing process reduces the tissue damage [28]. The excised LNs were ~5 mm in diameter. The excised LNs, deposited on a quartz plate for THz imaging, are shown in Fig. 1. THz imaging was first performed at −20 °C (below the water freezing temperature) and then at 20 °C (room temperature). An aluminum film was used for acquiring a reference signal. After the imaging, histological examination was performed to identify the metastatic states of the samples.
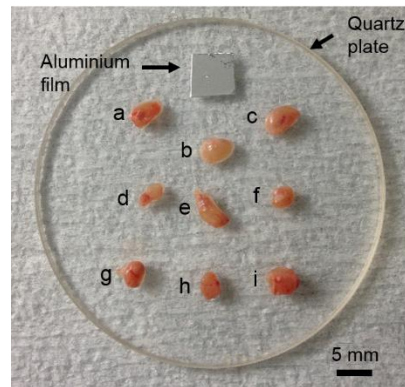
Fig. 1. Excised LNs on the quartz plate (a-c: LNs with no melanoma cells, d-f: LNs with melanoma cells for 15 days, g-i: LNs with melanoma cells for 30 days). The aluminum film was used for acquiring a reference signal.

The quartz plate and the aluminum film were in a temperature-controlled chamber (Fig. 2). A beam generated by a femtosecond laser was split into two using a beam splitter. One beam was used for eliciting THz radiation from a p-type doped InAs film, while the other beam was used for detecting the THz signal reflected from the sample, using a LT-GaAs photoconductive antenna. The detected THz time-domain waveform was Fourier-transformed into a frequency-domain spectrum (frequency range, 0–3 THz). THz images were acquired utilizing the raster motion of the sample stage in the sealed temperature-controlled chamber, and individual pixels were $50 \times 50$ $\mu m^2$ each. During the acquisition of images, the temperature in the chamber was constant ($-20$ °C and $20$ ° C for the low-temperature and room-temperature experiments, respectively). THz images of LNs were obtained by employing spectral analysis and signal processing methods. Signal processing was performed using Labview 2013 (ver. 13.0f2, National Instruments Co., Mopac Expwy, TX, USA).
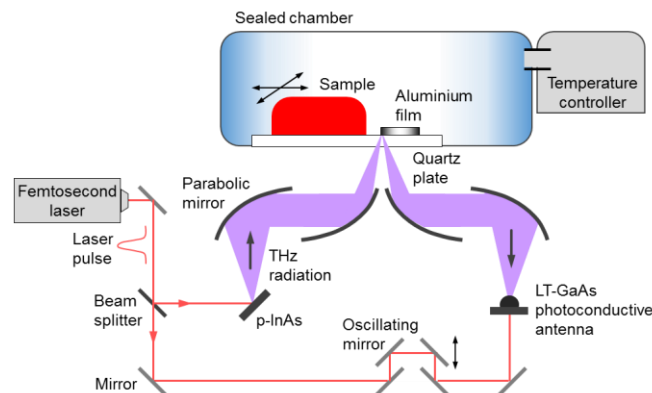


Fig. 2. Setup of the reflection-mode THz imaging system, with the temperature-controlled sample stage.

After the acquisition of THz images, the LNs were fixed in the formalin solution, dehydrated in the alcohol solution, and then dyed with hematoxylin and eosin staining. The metastatic states were validated using a microscope.

## 3. Results and analysis

Figure 3 shows the histological images of the representative samples, for the three groups of animals. The LNs of the animals without melanoma cells (Fig. 3(a)) are homogeneous and healthy. By contrast, the LNs of the animals injected with melanoma cells were completely

metastasized as tumor, 30 days after the injection (Fig. 3(b)). For both groups of LNs, the cell structures were uniform. However, the LNs of the animals injected with melanoma cells and monitored at 15 days after the injection (Fig. 3(c)) were not uniform and exhibited a clear boundary, separating intact cells (region c1 in Fig. 3(c)) from metastatic cells (region c2 in Fig. 3(c)). The boundary occurred owing to the proliferation of melanoma cells that were transferred with other nutrients from the blood.
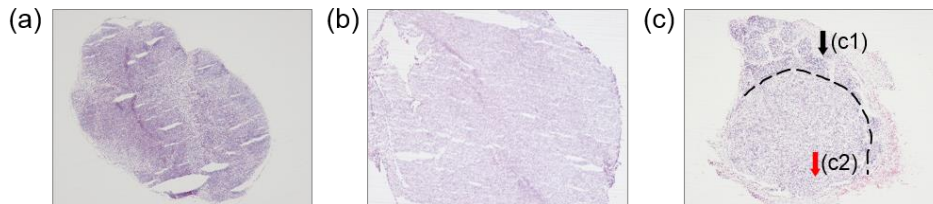


Fig. 3. Histological images of LNs. (a) A healthy LN, (b) a completely metastatic LN, and (c) a partially metastatic LN, with a boundary (dashed line) between (c1) the non-metastatic tissue and (c2) the region with melanoma cells.

Figure 4 shows the averaged (over animals) THz time-domain waveforms, obtained for the LNs of control animals and for completely metastatic LNs, along with their spectra. The THz signals acquired at 20 °C in Figs. 4(a) and 4(b) are very similar for the different LNs. The similarity was mostly owing to the strong absorption of water in the tissues. Figures 4(c) and 4(d) show the THz signals acquired for the same LNs at −20 °C. There is a small difference between the signals acquired from healthy and completely metastatic LNs with a relatively low signal-to-noise ratio, because the absorption by water was lower at the lower temperature; consequently, at the lower temperature the THz radiation was mostly affected by the tissue structure. We attempted to delineate the cancerous region based on this difference between the signals acquired from healthy and metastatic tissues.

THz imaging with pulsed radiation has been used for mapping images using the maximum ($E_{max}$) and minimum ($E_{min}$) of a THz temporal signal ($E(t)$) or using a refractive index and absorption coefficient of a THz spectral signal $E(\omega)$ [29–33]. For example, liver cancer samples embedded in paraffin yielded a 4% difference between the $E(\omega)$ signals acquired from normal and cancerous tissues, and cancerous regions were clearly detectable in these samples [22]. However, in the present study, the criteria based on $E_{max}$, $E_{min}$, and $E(\omega)$ were not satisfactory for determining the presence and shape of cancerous regions in partially metastatic LNs, because the corresponding $E(t)$ and $E(\omega)$ signals were very noisy.
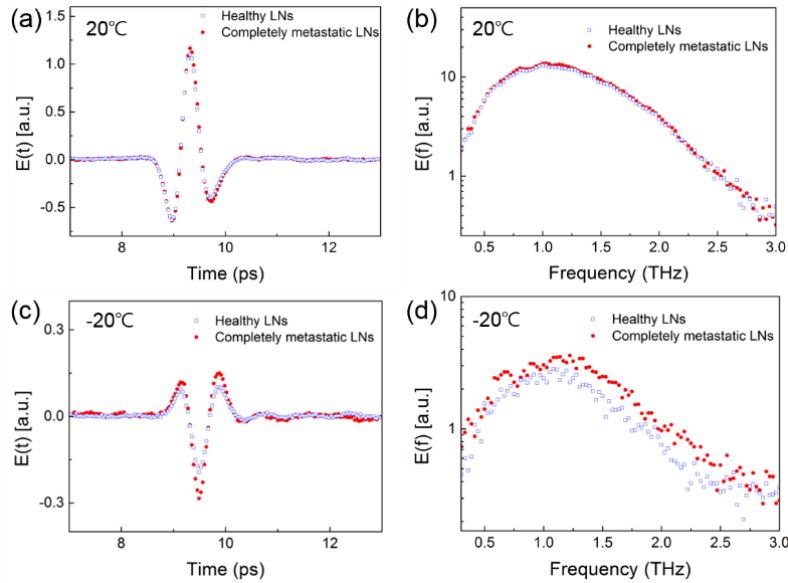
Fig. 4. THz time-domain waveforms and their Fourier spectra at 20 °C ((a) and (b)) and −20 °C ((c) and (d)).

A larger signal gap with less noise was required for obtaining images with clearly visible cancerous regions in partially metastatic LNs. After integration over the LN spectra, a stronger difference between signals was obtained, compared with those obtained any of the above-mentioned criteria, and normalization of the integrated spectra suggested the reference value for discriminating between normal and melanoma regions. The spectra were integrated using the following equation:

$$G_i = \int FT(E(t)_i)d\omega \qquad (1)$$

where $E(t)_i$ is the THz temporal signal and $G_i$ is the integration constant for the $i^{th}$ image pixel (i = 1,2,3…).The integrals were normalized as follows:

$$S_i = \frac{|G_i - G_{min}|}{G_{max} - G_{min}} \qquad (2)$$

where $G_{min}$ and $G_{max}$ are the minimum and maximum of $G_i$ and $S_i$ is the normalized result.

Figure 5 shows the distribution of $S_i$ for the different LNs. All of the distributions exhibit relatively high values of $S$, but the relative lower bounds are different. The distributions for the healthy LNs (Figs. 5(a), 5(b), and 5(c)) are characterized by lower minimal $S$ compared with those observed for the completely metastatic LNs (Figs. 5(d), 5(e), and 5(f)), while the minimal $S$ values for the partially metastatic LNs (Figs. 5(g), 5(h), and 5(i)) are between the values for the healthy and completely metastatic LNs. Owing to this separation, the lower bound on the $S$ values can be regarded as a criterion for discriminating between the normal and melanoma cells in LNs. Polynomial fits (red lines) to the different distributions clearly capture the differences between the different LNs.
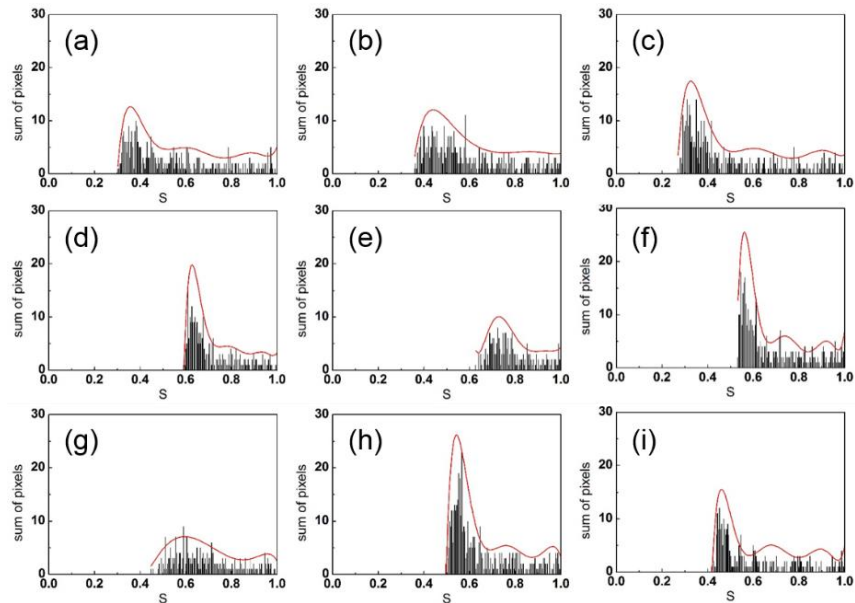
Fig. 5. Distributions of normalized integration factors for LNs (a-c: healthy LNs, d-f: completely metastatic LNs, g-i: partially metastatic LNs) at −20 °C (bar graph) and their polynomial fits (red curves).

Figure 6 shows the fits for the lower bound $S$ values for the healthy LNs (in Figs. 5(a), 5(b), and 5(c)) and completely metastatic LNs (in Figs. 5(d), 5(e), and 5(f)). The two families of curves can be separated by drawing a vertical line at $S = 0.53$. This value is a critical point for distinguishing between the two tissue states, and can be used as a reference for dichotomizing the LN images. Therefore, criteria based on spectral integration allow to clearly discriminate between healthy and metastatic regions in LNs.
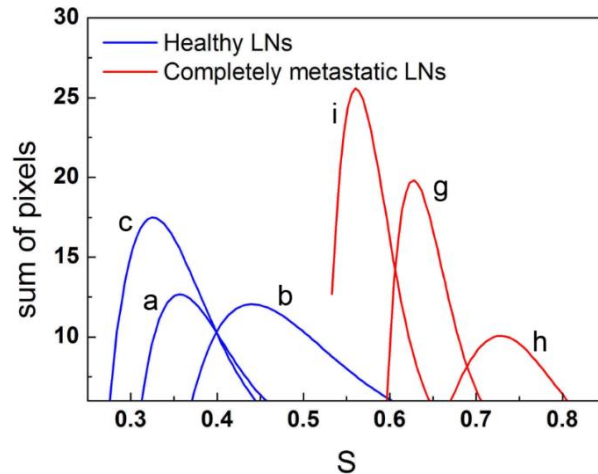


Fig. 6. Fits to $S$ distributions for the healthy LNs (a, b, and c) and completely metastatic LNs (g, h, and i), at −20 °C.

Figure 7 shows the photographs and THz images of the different LNs: (a) healthy LNs, (b) completely metastatic LNs, and (c) partially metastatic LNs. The photographs in Fig. 7 are the bottom views of the LNs. The THz images show that the different LNs have nearly the same shape, but frozen LNs are slightly smaller than those in the respective photographs. The THz

images are plotted using two colors that represent the areas with $S$ values higher and lower than the critical value. For measurements at room temperature, the THz images could not be colored according to the critical point, because at this temperature THz waves were strongly attenuated by water in the surface layers of tissue. However, cancerous regions in partially metastatic LNs are clearly visible at the low temperature (Fig. 7(c)). The boundary between the regions of different color in the color plots strongly correlated with the boundary between melanoma cells and healthy cells in histological images in Fig. 3(c).
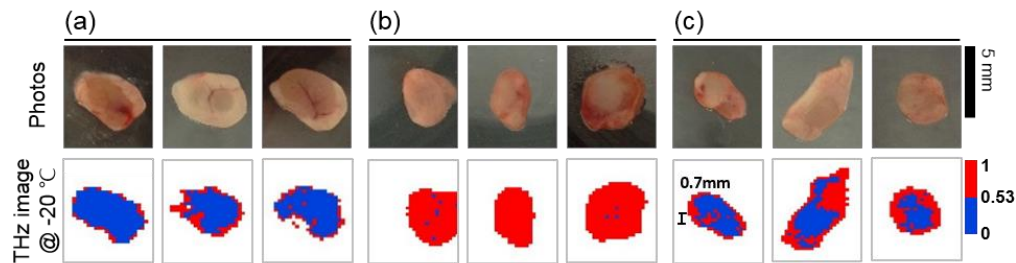


Fig. 7. THz imaging results for the three groups of LNs: (a) healthy LNs, (b) completely metastatic LNs, and (c) partially metastatic LNs. The bottom panel shows the THz images in two colors, corresponding to the normalized integration factor, $S$ being above or below the critical point of 0.53. The images successfully resolved a very small metastatic area with the linear dimension of ~0.7 mm.

The resolution of dichotomized THz images obtained using the spectral integration technique was sufficiently high to resolve a tiny metastatic area with the linear dimension of ~0.7 mm in the analyzed LNs. The technique can be applied at low temperatures (below the freezing temperature of water), and the results obtained using this technique are correlated with those obtained by histological examinations. The method is similar to the method of cryogenic pathologic examination that is used in the field of medicine and is advantageous because it is not time-consuming. THz imaging using the spectral integration technique (SIT) is likely to become an alternative or supplementing method for the early detection of small cancers. This novel method does not require staining and is feasible to monitoring the development of cancer.

## 4. Conclusion

In this pilot study, THz imaging with the SIT was used for differentiating the metastatic states of LNs, revealing cellular interfaces in partially metastatic LNs at the temperature below the freezing temperature of water. The SIT increased the contrast between the signals acquired from normal and melanoma regions with good image resolution. It enhanced the THz images with dichotomized coloring according to a critical value. The cellular interfaces in the dichotomized melanoma images were strongly correlated with the histological analysis results. The frozen THz imaging with the SIT is a simple technique but good enough to distinguish the difference between metastatic and normal lymph nodes without any complicated process. It is also promising as a supplementary technique for cryogenic pathologic examinations.

## Funding

## Acknowledgments